Front. Mech. Eng. 2022, 17(1): 1
https://doi.org/10.1007/s11465-021-0657-z

RESEARCH ARTICLE

Integrated slipper retainer mechanism to eliminate slipper wear in high-speed axial piston pumps

Qun CHAO[a,b], Junhui ZHANG (✉)[b], Bing XU[b], Qiannan WANG[b], Fei LYU[b], Kun LI[c]

[a] *State Key Laboratory of Mechanical System and Vibration, School of Mechanical Engineering, Shanghai Jiao Tong University, Shanghai 200240, China*
[b] *State Key Laboratory of Fluid Power and Mechatronic Systems, School of Mechanical Engineering, Zhejiang University, Hangzhou 310027, China*
[c] *Qing'an Group Co., Ltd, Xi'an 710077, China*
✉ *Corresponding author. E-mail: benzjh@zju.edu.cn (Junhui ZHANG)*

ABSTRACT The power density of axial piston pumps can greatly benefit from increasing the speed level. However, traditional slippers in axial piston pumps are exposed to continuous sliding on the swash plate, suffering from serious wear at high rotational speeds. Therefore, this paper presents a new integrated slipper retainer mechanism for high-speed axial piston pumps, which can avoid direct contact between the slippers and the swash plate and thereby eliminate slipper wear under severe operating conditions. A lubrication model was developed for this specific slipper retainer mechanism, and experiments were carried out on a pump prototype operating at high rotational speed up to 10000 r/min. Experimental results qualitatively validated the theoretical model and confirmed the effectiveness of the new slipper design.

KEYWORDS axial piston pump, high speed, slipper wear, slipper design, retainer, lubrication model

1 Introduction

Axial piston pumps play the role of "heart" in many hydraulic systems. They are widely used in the fields of construction, mining, automobile, and aerospace due to their high efficiency, great power density, available flow regulation, and long service life. Figure 1 illustrates the configuration of a typical swash plate type axial piston pump. The cylinder block contains multiple pistons at equal angular intervals about its centerline. Each piston is connected to a slipper through a ball-and-socket joint, which allows the slipper to rotate around the ball center. All the slippers rest on the swash plate, maintaining a reasonable contact with the swash plate by the retainer. The displacement chambers communicate with the pump ports through the valve plate openings. In addition, each displacement chamber connects itself to the slipper pocket by the orifices drilled in the slipper and the piston.

When the shaft drives the cylinder block via a spline mechanism, the slippers slide on the inclined swash plate and force the piston–slipper assemblies to reciprocate in the cylinder block. Low-pressure fluid flows into the displacement chamber as the piston is pulled out of the cylinder block. Conversely, high-pressure fluid flows out of the displacement chamber as the piston is pushed into the cylinder block. The two strokes repeat themselves for each revolution of the shaft, and the combined effect of individual pistons produces a continuous pumping action of the fluid. Three main lubricating interfaces are formed between the movable parts during the pump operation, including the slipper/swash plate interface, the piston/cylinder block interface, and the cylinder block/valve plate interface [1]. These lubricating interfaces have sealing and bearing functions and represent the main source of energy dissipation due to viscous friction and fluid leakage.

The axial piston pump is developed toward high power density by increasing its delivery pressure or rotational speed, especially in aerospace applications [2,3]. When the delivery pressure is limited by the system pressure and material strength, increasing the rotational speed can effectively improve the power density of axial piston pumps [4]. However, high rotational speed raises concerns about pump failure, especially about the slipper

Received April 17, 2021; accepted August 17, 2021

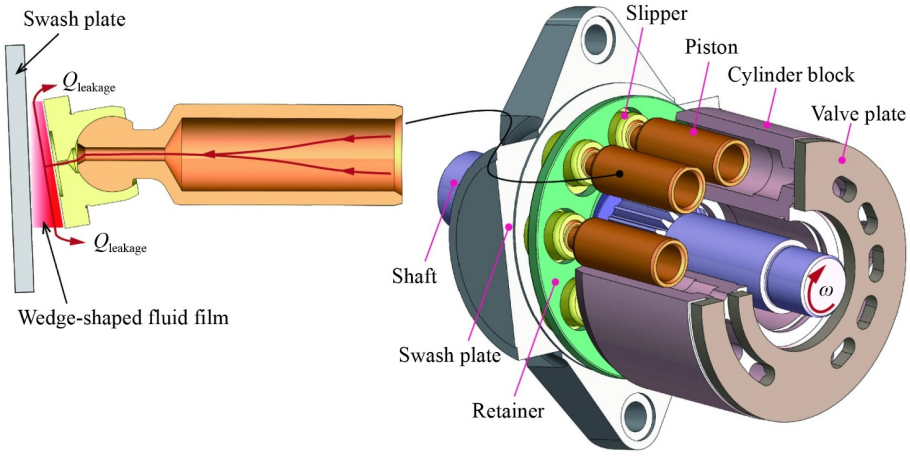

Fig. 1 Schematic of a swash plate type axial piston pump.

wear. First, the main pump kinematics requires the slippers to slide on the swash plate at high velocity, thereby causing severe sliding wear of the slippers when the pump operates at high rotational speeds. Second, high-speed rotation produces considerable centrifugal force and sliding friction acting on the slippers [5–7], leading to heavy tilting motion [8,9] and resulting in abrasion wear [10,11] of the slippers.

Some researchers have proposed some effective approaches to prevent slipper tilt. Manring et al. [8] considered that the slipper tilt could be avoided at high rotational speeds by increasing the hold-down force of the retainer. Hooke and Li [5] claimed that a small amount of convex surface on the slipper running face was essential for the successful operation of slippers. Xu et al. [10] reported that compared with the outer-slope sealing land, the inner-slope sealing land could decelerate the partial abrasion of the slippers. On the contrary, Jiang and Wang [11] confirmed that the outer-slope sealing land was beneficial to form stable fluid film and to prevent metal-to-metal contact between the slippers and the swash plate. Koç and Hooke [12] found that the slippers without orifice had greater resistance to the tilting couples than the standard ones with orifice.

In addition, other researchers focused on the wear mechanism of the slippers and the improvement methods in the wear resistance. Ma et al. [13] developed an elasto-hydrodynamic lubrication model to predict the slipper wear under different operating conditions. Wu et al. [14] revealed the effects of material properties on the temperature increase at the contact surfaces of the slipper bearing by comparing the tribological characteristics of different paired materials under dry friction conditions. Rizzo et al. [15] demonstrated that the nanocoating surface treatment reduced the friction coefficient of the slippers over a wide range of rotational speeds. Kalin et al. [16] discovered that the slippers with diamond-like carbon (DLC) coating had much lower wear against the swash plate than the standard ones. Schuhler et al. [17] experimentally confirmed the reduction in friction coefficient and wear rate for the slipper bearing by the W-doped DLC coating (DLC + WC) on the swash plate. In recent years, Ye et al. [18] and Tang et al. [19] have pointed out that the textured slippers can improve the lubrication performance and load-carrying capacity of the slipper bearing.

These efforts contribute remarkably to slipper wear reduction. However, the traditional slippers are still exposed to severe operating conditions because they must slide on the swash plate and suffer sliding wear. The worn slippers increase the vibration and noise [20] and reduce the efficiency and lifetime of the pump. Therefore, this paper aims to present a new integrated slipper retainer mechanism that can almost eliminate the slipper wear in high-speed axial piston pumps.

2 Structure description

Figure 2 shows an integrated slipper retainer mechanism for a high-speed axial piston pump. Different from the traditional slipper retainer mechanism, the new mechanism is an integrated unit that enables the slippers to be free from sliding on the swash plate. Instead, the rotating retainer slides against the stationary bearing plate that is embedded within the swash plate. The new retainer consists of three parts, namely, the driving plate, the adjusting plate, and the sliding plate. The three plates are assembled together using a group of bolts. The top driving plate is driven by the multiple slippers that rotate along with the cylinder block. The middle adjusting plate adjusts the maximum clearance between the slipper and the sliding plate that is usually on the order of micrometers in magnitude [21]. The bottom sliding plate rotates against the bearing plate, and their reasonable contact is controlled by the spherical cup.

When the retainer rotates against the bearing plate, a critical lubricating interface is formed between them, i.e.,

the sliding plate/bearing plate interface, as shown in Fig. 3. The pressurized fluid is supplied from the displacement chamber to the kidney-shaped pocket in the sliding plate through the small holes drilled in the piston, slipper, and sliding plate. Then, the supplied fluid leaks from the pockets into the pump casing through the small gap between the sliding and bearing plates, generating hydrostatic pressure across the lubricating interface. At the same time, the rotation of the sliding plate produces additional hydrodynamic pressure. The combined hydrostatic and hydrodynamic pressures balance other external forces and moments acting on the sliding plate.

This description shows that the integrated slipper retainer mechanism differs significantly from the traditional one in terms of kinematics and force balance. First, the slippers in the new mechanism no longer slide on the swash plate. Instead, they only serve to drive the integrated retainer and to provide oil passages for the sliding plate/bearing plate interface. In fact, the sliding plate replaces the traditional slippers to slide on the bearing plate or swash plate. The driving plate and adjusting plate act as a retaining device to pull the slippers out of the cylinder block during the suction stroke. Second, the clamping forces from the pistons are carried by the sliding plate bearing instead of the multiple slipper bearings. This new configuration reduces the risk of slipper failure under extreme conditions by eliminating the sliding motion of the slippers on the swash plate. In this case, the tribological contacts have been transformed from the traditional slipper/swash plate interface to the sliding plate/bearing plate interface. Therefore, a lubrication model is necessary for the sliding

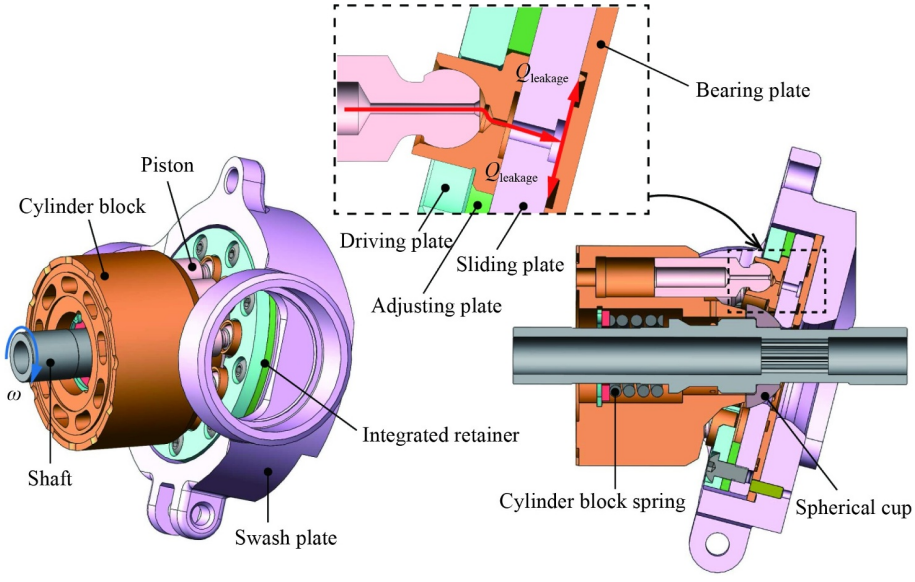

Fig. 2 Configuration of the new slipper retainer mechanism for a high-speed axial piston pump.

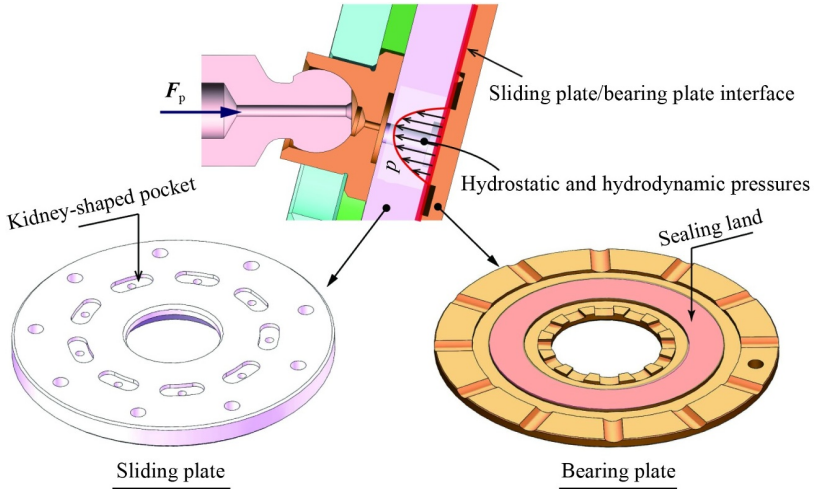

Fig. 3 Illustration of the sliding plate/bearing plate interface.

plate/bearing plate interface during the design phase.

3 Lubrication model

In this section, we develop a lubrication model for the sliding plate/bearing plate interface to examine its tribological performance, including the gap height distribution, the pressure distribution, and the sliding plate attitude. Similar to the slipper/swash plate interface, a reasonable gap height between the sliding and bearing plates is essential to the integrated slipper retainer mechanism. On the one hand, a large gap height increases the gap leakage and reduces the volumetric efficiency of the pump. One the other hand, a small gap height is likely to cause metal-to-metal contact between the sliding and bearing plates, leading to abrasion wear and potential pump failure.

The sliding plate attitude relative to the bearing plate can be represented by the gap heights at three points, P_1, P_2, and P_3, as shown in Fig. 4. The three points are located at 120° intervals at the outer diameter of the sealing land. Points P_1 and P_2 are located at the high-pressure (HP) and low-pressure (LP) sides, respectively, and point P_3 is located at the bottom dead center (BDC). Assuming that the sliding and bearing plates are rigid bodies, any gap height $h(r, \theta)$ between them can be expressed by the gap heights at the three points given by the vector $\boldsymbol{h} = (h_1, h_2, h_3)$ [10], as follows:

$$h(r,\theta) = \frac{1}{\sqrt{3}R_4}(h_1 - h_2) r\sin\theta + \frac{1}{3R_4}(2h_3 - h_1 - h_2) r\cos\theta + \frac{1}{3}(h_1 + h_2 + h_3), \quad (1)$$

where r is the radial distance from the coordinate origin, θ is the angular distance from the y axis, and R_4 is the outer radius of the external sealing land.

The gap height across the lubricating interface depends on the balance between two types of external forces acting on the sliding plate. The first external force is the clamping force from individual piston–slipper assemblies and the spherical cup. The clamping force includes four parts, namely, friction force between the piston and the cylinder bore F_f, pressure force from the displacement chamber F_d, reciprocating inertial force of the piston–slipper assembly F_a, and spring force exerted by the spherical cup F_s. The second external force is the separating force generated by the fluid film.

The vector form of the total clamping force $\boldsymbol{F}_c$ can be expressed as follows:

$$\boldsymbol{F}_c = \frac{1}{\cos\beta}\begin{bmatrix} 0 & 0 & -F_s + \sum_{i=1}^{9}(F_{fi} + F_{di} + F_{ai}) \end{bmatrix}^T, \quad (2)$$

where β is the swash plate angle, and the subscript i denotes the ith piston.

The friction force of the ith piston can be expressed as follows [22]:

$$F_{fi} = f_p \frac{v_{pi}}{V_{pi}}(N_{1i} + N_{2i}) = f_p \frac{v_{pi}}{V_{pi}} \frac{\tan\beta[2L - l_i - 2f_p r_p(v_{pi}/V_{pi})](-m_p a_{pi} + F_{di})}{l_i - f_p \tan\beta[2L - l_i - 2f_p r_p(v_{pi}/V_{pi})](v_{pi}/V_{pi})}, \quad (3)$$

where N_{1i} and N_{2i} are the contact forces between the ith piston and the cylinder bore at two engaging ends, L is the piston length, l_i is the contact length of the ith piston within the cylinder bore, r_p is the piston radius, m_p is the piston mass, f_p is the friction coefficient between the piston and the cylinder bore, v_{pi} and a_{pi} are the velocity and acceleration of the ith piston along its centerline, respectively, and V_{pi} is the resultant velocity of the ith piston relative to the cylinder block.

The velocity and acceleration of the ith piston along its centerline are given by the following [23]:

$$v_{pi} = \omega R_p \tan\beta \sin\varphi_i, \quad (4)$$

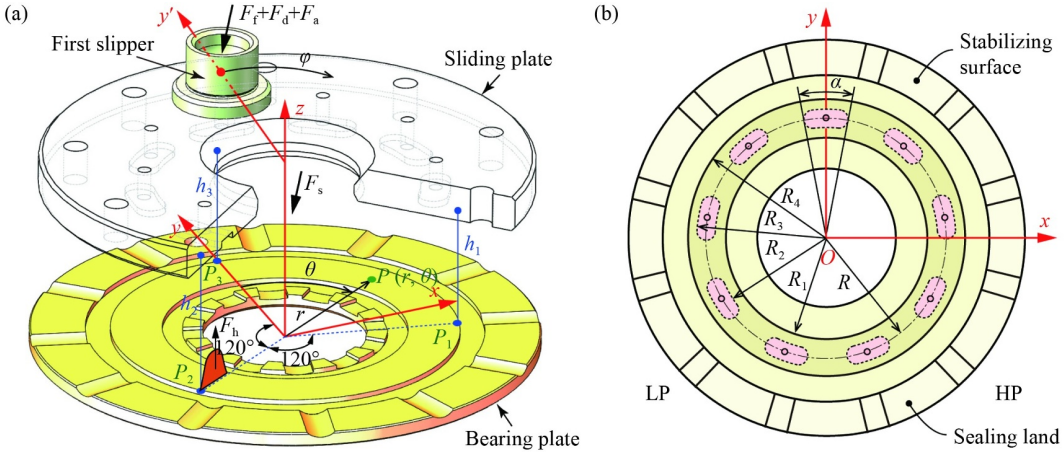

Fig. 4 (a) Lubricating interface between sliding and bearing plates; (b) tribological surface of the bearing plate.

$$a_{pi} = \omega^2 R_p \tan\beta \cos\varphi_i, \tag{5}$$

where ω is the rotational speed of the pump, R_p is the piston pitch radius, and φ_i is the angular displacement of the ith piston from the BDC.

The resultant velocity of the ith piston relative to the cylinder block can be written as follows:

$$V_{pi} = \sqrt{v_{pi}^2 + (\omega_{pi} r_p)^2}, \tag{6}$$

where ω_{p_i} is the spinning speed of the ith piston that is determined by the following equation [22]:

$$J_p \dot{\omega}_{pi} = -f_b F_{bi} r_b \cos\beta - f_p r_p (N_{1i} + N_{2i}) \frac{\omega_{pi} r_p}{V_{pi}}, \tag{7}$$

where J_p is the piston's moment of inertia about its axis, r_b is the piston ball radius, f_b is the friction coefficient between the piston ball and the slipper socket, and F_{bi} is the contact force between the ith piston ball and the slipper socket.

$$F_{bi} = \frac{F_{ai} + F_{di}}{\cos\beta - \dfrac{\sin\beta}{l_i} f_p \left(2L - l_i - f_p r_p \dfrac{v_{pi}}{V_{pi}}\right) \dfrac{v_{pi}}{V_{pi}}}. \tag{8}$$

The contact length of the ith piston within the cylinder bore in Eqs. (3) and (8) can be expressed by

$$l_i = l_0 + R_p (1 - \cos\varphi_i) \tan\beta, \tag{9}$$

where l_0 is the initial contact length of the first piston.

The pressure force for the ith piston in Eqs. (3) and (8) is

$$F_{di} = -\pi r_p^2 p(\varphi_i), \tag{10}$$

where $p(\varphi_i)$ represents the ith displacement chamber pressure as a function of the angular displacement.

The reciprocating inertial force of the ith piston−slipper assembly is

$$F_{ai} = -m a_{pi} = -m\omega^2 R_p \tan\beta \cos\varphi_i, \tag{11}$$

where m is the mass of one piston–slipper assembly.

The moment generated by the total clamping force $\boldsymbol{M}_c$ can be given in matrix form as follows:

$$\boldsymbol{M}_c = \begin{pmatrix} M_x & M_y & 0 \end{pmatrix}^T. \tag{12}$$

The moment components in Eq. (12) can be written as follows:

$$M_x = \frac{R}{\cos\beta} \sum_{i=1}^{9} (F_{fi} + F_{di} + F_{ai}) \cos\varphi_i, \tag{13}$$

$$M_y = -\frac{R}{\cos\beta} \sum_{i=1}^{9} (F_{fi} + F_{di} + F_{ai}) \sin\varphi_i, \tag{14}$$

where M_x and M_y are the moment components of $\boldsymbol{M}_c$ in the x and y directions, respectively, and R is the pitch radius of the kidney-shaped pockets in the sliding plate.

The clamping force and moment should be counteracted by the separating force $\boldsymbol{F}_h$ and its moment $\boldsymbol{M}_h$.

$$\boldsymbol{F}_h = \begin{pmatrix} 0 & 0 & \int_0^{2\pi} \int_{R_1}^{R_4} pr \mathrm{d}r \mathrm{d}\theta \end{pmatrix}^T, \tag{15}$$

$$\boldsymbol{M}_h = \begin{pmatrix} \int_0^{2\pi} \int_{R_1}^{R_4} pr^2 \cos\theta \mathrm{d}r \mathrm{d}\theta & -\int_0^{2\pi} \int_{R_1}^{R_4} pr^2 \sin\theta \mathrm{d}r \mathrm{d}\theta & 0 \end{pmatrix}^T. \tag{16}$$

Equations (15) and (16) involve the pressure distribution across the lubricating interface that are governed by the following Reynolds equation [24], as follows:

$$\frac{1}{r}\frac{\partial}{\partial r}\left(\frac{rh^3}{\mu}\frac{\partial p}{\partial r}\right) + \frac{1}{r^2}\frac{\partial}{\partial\theta}\left(\frac{h^3}{\mu}\frac{\partial p}{\partial\theta}\right) = 6\frac{1}{r}\frac{\partial(v_\theta h)}{\partial\theta} - 12\frac{v_\theta}{r}\frac{\partial h}{\partial\theta} + 12\frac{\partial h}{\partial t}, \tag{17}$$

where μ is the fluid dynamic viscosity, and t is time.

Considering $v_\theta = \omega_s r$, Eq. (17) can be further expressed as follows:

$$\frac{1}{r}\frac{\partial}{\partial r}\left(\frac{rh^3}{\mu}\frac{\partial p}{\partial r}\right) + \frac{1}{r^2}\frac{\partial}{\partial\theta}\left(\frac{h^3}{\mu}\frac{\partial p}{\partial\theta}\right) = -6\omega_s\frac{\partial h}{\partial\theta} + 12\frac{\partial h}{\partial t}, \tag{18}$$

where ω_s is the rotational speed of the sliding plate that is approximately equal to the rotational speed of the pump.

The pressure boundary conditions for the Reynolds equation in Eq. (18) are as follows:

$$p(R_2 \leqslant r \leqslant R_3, -\alpha/2 + \varphi_i \leqslant \theta \leqslant \alpha/2 + \varphi_i) = p(\varphi_i), \tag{19}$$

$$p(r = R_1, 0 \leqslant \theta \leqslant 2\pi) = p(r = R_4, 0 \leqslant \theta \leqslant 2\pi) = p_c, \tag{20}$$

where α is the angular span of the kidney-shaped pockets in the sliding plate, and p_c is the casing pressure of the pump.

Figure 5 illustrates the simulation model structure for the sliding plate/bearing plate interface by a basic flow diagram. The numerical computation is completed by the software package MATLAB. The initial gap heights, operating conditions, and geometry parameters of the pump serve as inputs to the Reynolds equation. The partial differential Reynolds equation can only be solved analytically in some simple cases. We used the finite volume method to create a number of grids for numerically solving the Reynolds equation due to its popularity in the computational fluid dynamics community. The fluid in the sliding plate/bearing plate interface is divided into two regions, as follows: one is the fluid film across the sealing land, and the other is the pressurized fluid in the kidney-shaped pockets. The Reynolds equation is solved to output the pressure distribution in the interface, during which two pressure boundary conditions are required for the solution. The first boundary pressure is the casing pressure that is assumed to be constant. The second boundary pressure is the pocket pressure of the sliding plate that is considered as a lumped parameter and approximately equal to the displacement chamber pressure. The transient displacement chamber pressure should be solved by a separate pressure model prior to simulation. The details about the

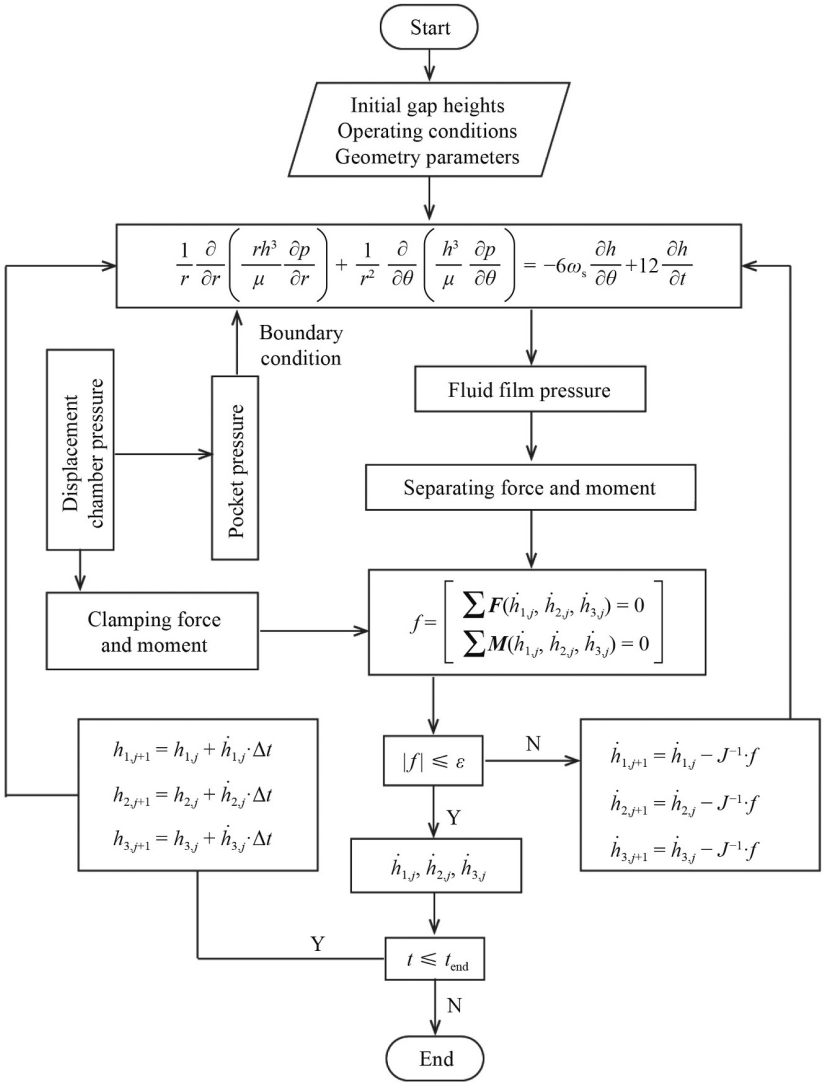

Fig. 5 Program structure of the simulation algorithm for the sliding plate/bearing plate interface.

displacement chamber pressure model can be found in Ref. [25].

We can calculate the separating force and moment generated by the sliding plate/bearing plate interface after obtaining the pocket pressure and the pressure distribution across the sealing land. The clamping force and moment are determined by the pump kinematics and the displacement chamber pressure. The force and moment balance of the sliding plate may not be satisfied at the initial step of simulation. In this case, the gap heights at the three points and their shifting velocities are self-adjusted to update the pressure distribution until the force and moment balance conditions are achieved. Once the gap height $\boldsymbol{h} = (h_1, h_2, h_3)$ is obtained, the gap height distribution across the interface is determined because the gap height at any point can be calculated by Eq. (1). Furthermore, the attitude of the sliding plate relative to the bearing plate can be expressed in terms of minimum or maximum gap height, azimuth angle, and tilting angle.

Solving the equation $\left.\frac{\partial h(r,\theta)}{\partial \theta}\right|_{r=R_4}=0$ yields the azimuth angle (θ_a) of the minimum or maximum gap height.

$$\theta_{a1,2}=\arctan\frac{\sqrt{3}(h_1-h_2)}{2h_3-h_1-h_2}. \tag{21}$$

Two available azimuth angles satisfy Eq. (21); one azimuth angle is associated with the minimum gap height, and the other azimuth angle is associated with the maximum gap height. Substituting Eq. (21) into Eq. (1) with $r = R_4$ yields the minimum and maximum gap height:

$$h_{min}=\min\{h(R_4,\theta_{a1}),h(R_4,\theta_{a2})\}, \tag{22}$$

$$h_{max}=\max\{h(R_4,\theta_{a1}),h(R_4,\theta_{a2})\}. \tag{23}$$

Then, the tilting angle of the sliding plate relative to the bearing plate is given by

$$\gamma=\arctan\frac{h_{max}-h_{min}}{2R_4}. \tag{24}$$

4 Simulation and experimental results

Table 1 lists the main geometrical dimensions and fluid properties of the reference pump for the simulation. All the simulation results are presented under steady-state conditions after three revolutions of the pump. Figure 6 shows the simulation results for the gap heights of the three points at two different rotational speeds. The gap height at each point varies slightly over a cycle, which indicates that the sliding plate runs steadily against the bearing plate. The gap height at point P_1 at the HP side is much larger than that at point P_2 at the LP side, which implies that the sliding plate is tilted toward the LP side. As the rotational speed rises from 5000 to 10000 r/min, both the gap heights at points P_1 and P_2 increase because of the hydrodynamic effect. Interestingly, the gap height difference between points P_1 and P_2 becomes smaller at 10000 r/min than at 5000 r/min. Such variation of the gap height with the rotational speed reduces the tilting behavior of the sliding plate, which can help the integrated slipper retainer mechanism survive at high rotational speeds.

Figure 7 shows an example of the gap height and pressure distributions across the sliding plate/bearing plate interface at angular displacements of 90° and 270°. The sliding plate is tilted toward the LP side, leading to a large gap height at the HP side and a small gap height at the LP side, as shown in Figs. 7(a) and 7(c). The rotation of the tilted sliding plate generates local hydrodynamic pressure at the LP side, as shown in Figs. 7(b) and 7(d), which in turn helps reduce the tilting motion of the sliding plate. Figure 8 shows the variation of the tilting angle of the sliding plate with the angular displacement. The tilting angle of the sliding plate varies slightly over a cycle and even decreases slightly when the rotational speed increases from 5000 to 10000 r/min.

Limiting the tilting angle of the sliding plate at high rotational speeds is essential because excessive tilting motion causes a rather small minimum gap height and thus undesirable metallic contact. Figure 9 highlights the minimum gap height and its azimuth angle in the sliding plate/bearing plate interface over one cycle. The minimum gap height is only about 1 μm and it occurs near the middle of the LP side (i.e., $\theta_a = 270°$), which can be explained by the difference of pressure distribution between the HP and LP sides (Figs. 7(b) and 7(d)). The tilting motion of the sliding plate may lead to metal-to-metal contact between the sliding and bearing plates at the middle of the LP side if the minimum gap height becomes excessively small. In addition, when the rotational speed rises from 5000 to 10000 r/min, the minimum gap height becomes larger due to the increased hydrodynamic separating force.

To evaluate the effectiveness of the integrated slipper retainer mechanism, we developed a high-speed axial piston pump prototype (Fig. 10(a)) and built a test rig (Fig. 10(b)) for it. The pump prototype was a nine-piston swash-plate-type axial piston pump with variable displacement ranging from 0.6 to 7.25 mL/r. The maximum discharge pressure and rotational speed of the pump prototype were 28 MPa and 10000 r/min, respectively. As shown in Fig. 10(c), the charge pump supplied pressurized oil for the high-speed pump prototype when they are driven by two separate electric motors. The outlet pressure of the pump prototype was controlled by the pressure relief valve. Pressure and temperature sensors were installed at the inlet port, outlet port, and drain ports to measure the oil temperature and pressure at these pump ports. Two flow meters were separately installed in the drain line and outlet line to monitor the leakage and delivery flow rates, respectively. Further details about the sensors of the test rig can be found in Ref. [26].

The pump prototype was equipped with the new and traditional slipper retainer devices in turn after minor modification, as shown in Fig. 11. The other parts of the pump prototype remained unchanged except for the slipper retainer device. Compared with the new slipper

Table 1 Main geometrical dimensions and fluid properties of the high-speed axial piston pump

Variable	Value	Variable	Value
Angular span of kidney-shaped pocket, α/(°)	28	Casing pressure, p_c/MPa	0.05
Swash-plate angle, β/(°)	5	Outlet pressure, p_H/MPa	20
Fluid dynamic viscosity, μ/(Pa·s)	0.012	Inlet pressure, p_L/MPa	0.5
Fluid density, ρ/(kg·m^{-3})	837	Pitch radius of kidney-shaped pockets, R/mm	20.35
Spring force, F_s/N	320	Piston pitch radius, R_p/mm	20
Piston's moment of inertia, J_p/(kg·mm^2)	0.16	Inner radius of internal sealing land, R_1/mm	16.3
Piston length, L/mm	26	Outer radius of internal sealing land, R_2/mm	17.8
Initial contact length of the first piston, l_0/mm	14.5	Inner radius of external sealing land, R_3/mm	23
Mass of piston-slipper assembly, m/g	16.5	Outer radius of external sealing land, R_4/mm	24.5
Piston mass, m_p/g	12	Piston ball radius, r_b/mm	3.75
Number of pistons, N	9	Piston radius, r_p/mm	5

retainer device, the traditional one removed the driving plate, the adjusting plate, and the sliding plate, and its slippers directly slid on the bearing plate that was embedded in the swash plate. Hard and soft paired materials were selected for the tribological parts in these two different slipper retainer devices. Specifically, in the traditional slipper retainer device, the materials of the slippers and the bearing plate were HMn58-2 and 38CrMoAlA, respectively, while in the new slipper retainer device, the materials of the sliding plate and the bearing plate were 38CrMoAlA and HMn58-2, respectively. The same experimental procedure was performed on the pump prototype with different slipper retainer devices. The pump displacement was fixed to about 2 mL/r during the experimental process. The pump prototype operated at a constant rotational speed of 10000 r/min and discharge pressure of 20 MPa. The oil temperature at the pump inlet was kept at (32 ± 1) °C to eliminate its influence on the pump performance.

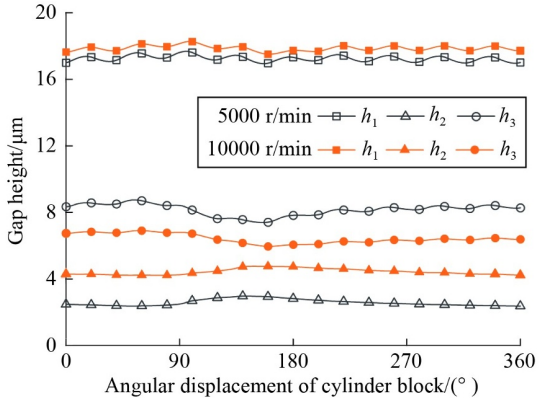

Fig. 6 Gap height at the three points at different rotational speeds (discharge pressure = 20 MPa).

The pump prototype was disassembled after tests and the sliding surfaces were examined, as shown in Fig. 12. For the new integrated slipper retainer mechanism (Fig. 12(a)), almost no visible sliding wear was found on the sliding plate surface, while a slight scratch could be found near the outer edge of the bearing plate at the LP side. This slight scratch might have resulted from accidental metallic contact between the sliding and bearing plates caused by the micro-tilting motion of the sliding plate. In addition, the sealing land of the bearing plate was somewhat black near the middle of the LP side, i.e., θ_a = 270°. This finding could be explained by the minimum gap height near the middle of the LP side, and therefore, the strengthened shearing effect generated "hot spots" at that location [27]. The witness marks on the bearing plate qualitatively validated the simulation results of the minimum gap height and its azimuth angle for the sliding plate/bearing plate interface (Figs. 7 and 9).

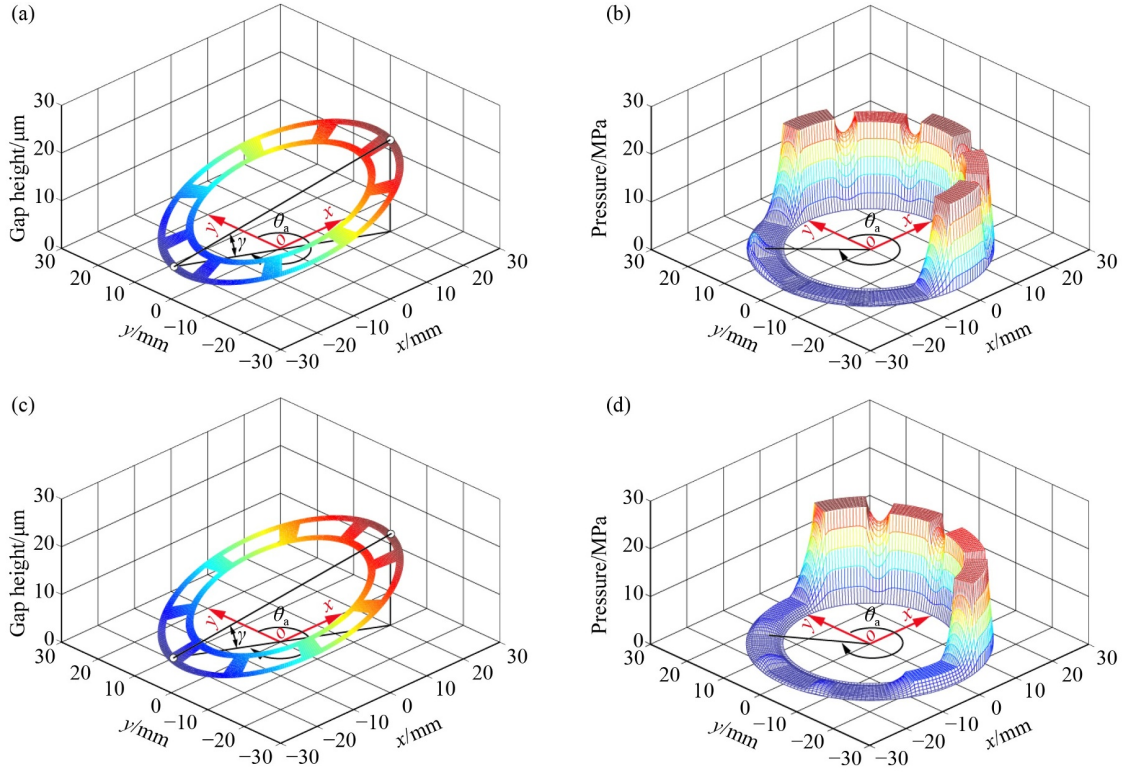

Fig. 7 Gap height and pressure distributions across the sliding plate/bearing plate interface (discharge pressure = 20 MPa, rotational speed = 10000 r/min). (a) Gap height distribution at 90°; (b) pressure distribution at 90°; (c) gap height distribution at 270°; and (d) pressure distribution at 270°.

The slippers in the new slipper retainer device had almost no visible wear on their running surface as expected (Fig. 12(b)) because they no longer slid on the swash plate or bearing plate. In contrast, the slippers in the traditional slipper retainer device suffered severe partial abrasion at their outer edges (Fig. 12(c)). This phenomenon occurred because the tilted slippers in the traditional design were exposed to high-velocity sliding on the bearing plate, resulting in serious metallic contact between the slippers and the bearing plate. As a result, the soft brass was transferred from the slipper to the bearing plate. The partial abrasion decreased the load-carrying capacity of the lubricating interface [10] and further increased the metallic contact between the slippers and the bearing plate. The metallic contact would generate more heat and increase the temperature of the drainage oil. After a test that lasted about 10 min, the oil temperature rise between the drain and inlet ports decreased from 39.5 °C to 14.3 °C when the pump prototype was equipped with the new integrated slipper retainer device instead of the traditional one.

5 Discussion

The presented integrated slipper retainer mechanism enables the traditional slippers to get rid of high-velocity sliding on the bearing plate or swash plate, which thereby eliminates the common slipper failure due to partial abrasion. The clamping force from the pistons is now counteracted by the separating force generated within the sliding plate/bearing plate interface instead of the traditional slipper/swash plate interface. When the sliding plate rotates against the bearing plate at high rotational speeds, the sliding plate has a steady attitude relative to the bearing plate over a cycle (Figs. 8 and 9). The small variation of the minimum gap height over a cycle is beneficial to reduce the metallic contact between the sliding and bearing plates at high rotational speeds. In contrast, the gap height and tilting angle of the traditional slippers at high rotational speeds usually fluctuate significantly over a cycle due to the centrifugal effect and the rapid switch between high and low pressures [21,28]. This fluctuation of the slipper attitude is likely to cause a serious partial abrasion of the slippers, leading to reduced volumetric and mechanical efficiencies and even sudden pump failure.

In addition to eliminating the sliding motion of traditional slippers, the integrated slipper retainer mechanism also acts as a “fixed-clearance” retainer that holds the slippers against the top surface of the sliding plate and prevents the slippers from being tilted heavily at high rotational speeds [29]. The slippers in the new mechanism are still a leakage source although they no longer engage in sliding motion on the swash plate. The “fixed-clearance” function increases the resistance to the slipper tilt at high rotational speeds and hence decreases the slipper leakage caused by wedge-shaped fluid film. In addition, the slippers in the present work are designed to be overclamped [12,30], which also helps reduce the tilting motion of the slippers.

The lubrication model for the sliding plate/bearing plate interface does not consider the sophisticated

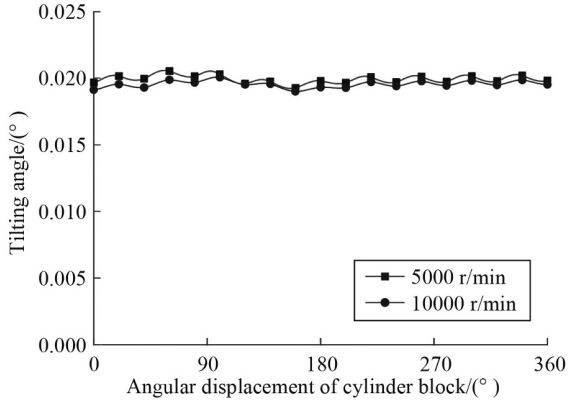

Fig. 8 Tilting angle of the sliding plate relative to the bearing plate interface (discharge pressure = 20 MPa).

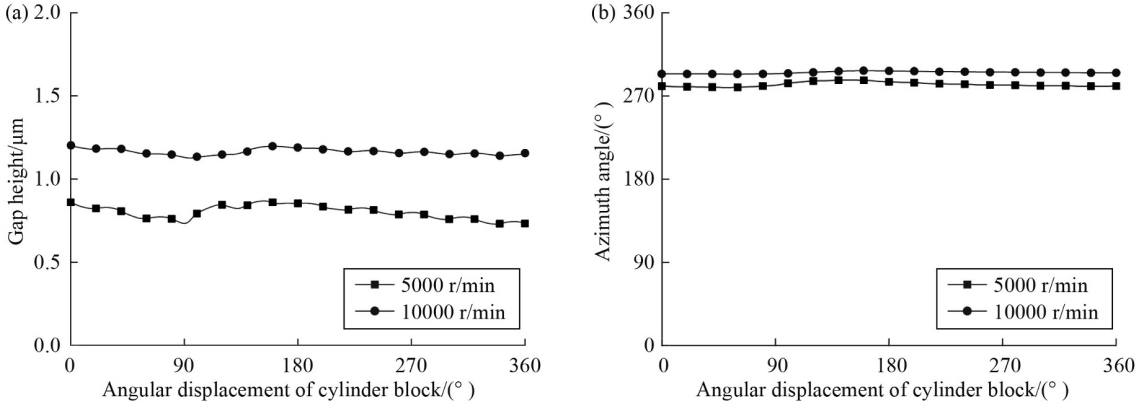

Fig. 9 (a) Minimum gap height and (b) its azimuth angle in the sliding plate/bearing plate interface (discharge pressure = 20 MPa).

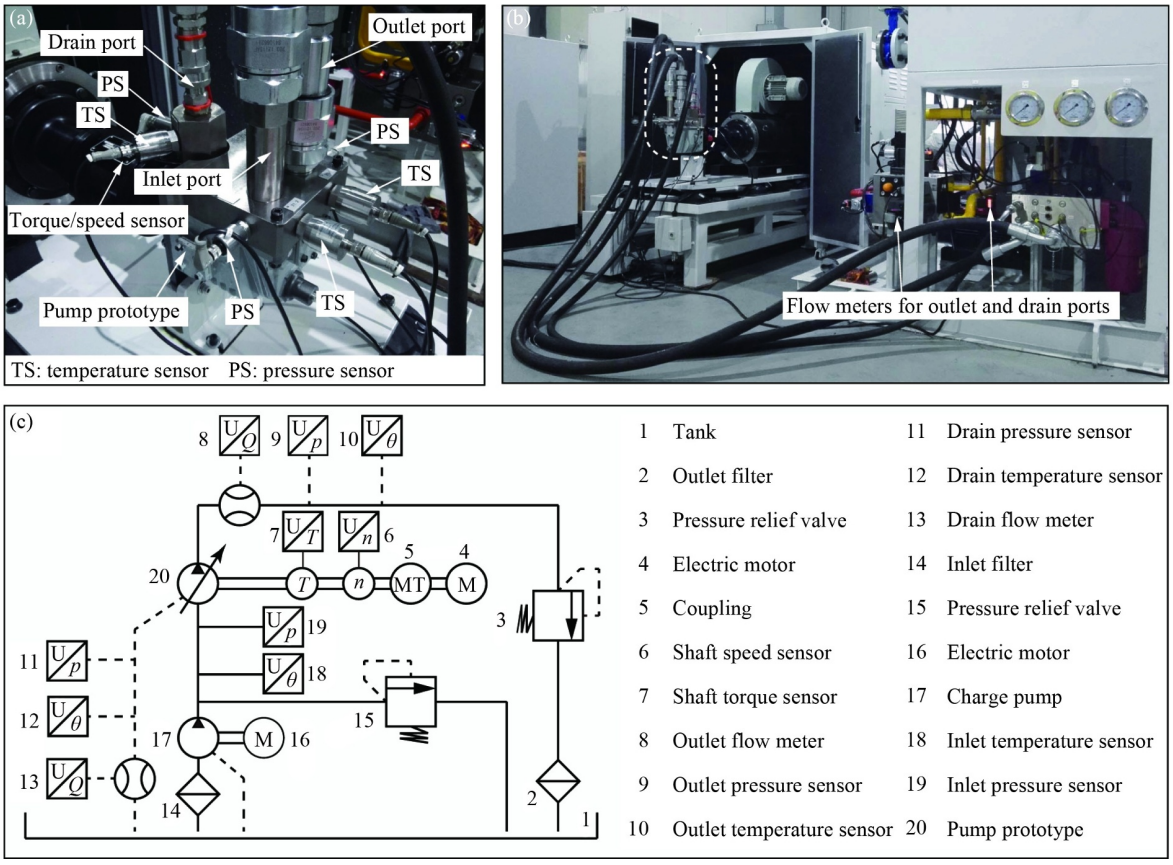

Fig. 10 (a) High-speed pump prototype; (b) test rig; (c) hydraulic circuit schematic. Reproduced from Ref. [26] with permission from Springer Nature.

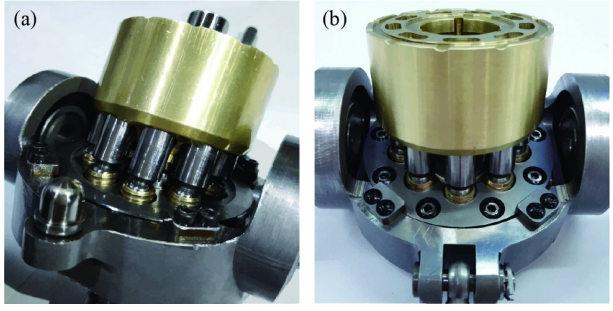

Fig. 11 Pump prototype equipped with (a) traditional slipper retainer device and (b) new slipper retainer device.

fluid–structure–thermal interaction problem. In axial piston pumps, the pressure and thermal deformations of movable parts influence the pressure distribution across the lubricating interfaces by changing the gap height [31–33]. Likewise, the sliding and bearing plates in the new slipper retainer mechanism can also experience pressure and thermal deformations, which in turn generates additional hydrodynamic effects and increases the load-carrying capacity of the interface [34,35]. This condition may explain why the sliding and bearing plates do not suffer severe wear (Fig. 12(a)) even though the minimum gap height between them was small (Fig. 9(a)).

However, possible metallic contact may happen between the sliding and bearing plates if the minimum gap height is excessively small. In addition, the minimum gap height tends to cause a local thermal problem near the middle of the LP side (Fig. 12(a)) due to the strengthened shearing effect. Therefore, boundary friction and thermal deformation are the potential weakness of the sliding plate/bearing plate interface at high rotational speeds and high operating pressures. This potential weakness can be partially overcome by increasing the load-carrying capacity or anti-wear resistance of the interface, such as coating [16,17], new paired materials [14], and surface texturing [18,19].

6 Conclusions

Slipper wear is a common failure mode for high-speed axial piston pumps because of the sliding and tilting motions of the slippers on the swash plate. The integrated slipper retainer mechanism presented in this work successfully eliminates slipper wear by avoiding the high-velocity sliding motion of the slippers. The clamping force from the pistons is now balanced by the hydrostatic and hydrodynamic pressures within the sliding

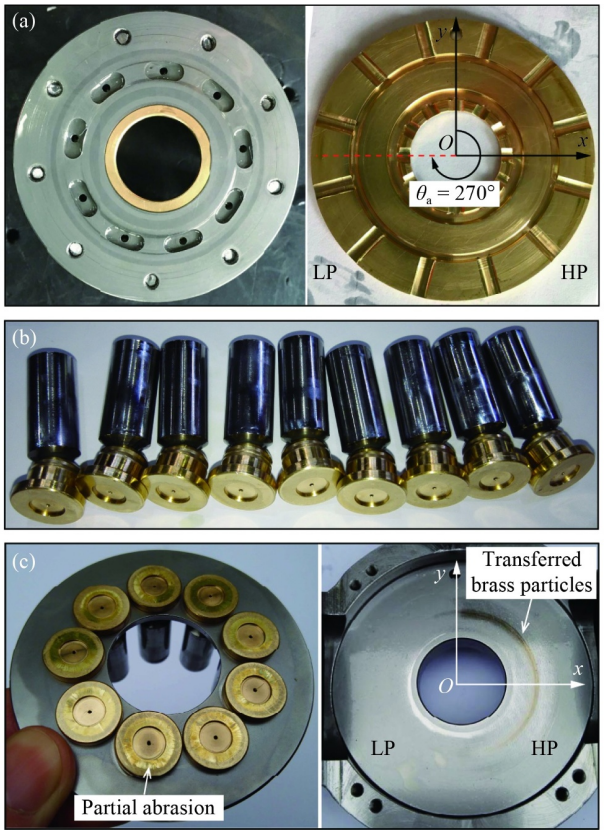

Fig. 12 Comparison of the sliding wear between two types of slipper retainer mechanisms. (a) Sliding plate and bearing plate in the new mechanism; (b) slippers in the new mechanism; (c) slippers and bearing plate in the traditional mechanism.

plate/bearing plate interface instead of the traditional slipper/swash plate interface. The hydrostatic design of the sliding plate/bearing plate interface can be realized in other forms, in addition to the present kidney-shaped pockets in the sliding plate and circular sealing land in the bearing plate. For example, the hydrostatic principle may be achieved by machining a number of circular pockets and sealing lands at the bottom surface of the sliding plate [36]. This alternative design looks like a special sliding plate that integrates multiple traditional slipper bearings at its running surface.

A lubrication model is developed to predict the tribological behavior of the sliding plate/bearing plate interface, including the gap height and pressure distributions, and the attitude of the sliding plate relative to the bearing plate. The simulation results show that the minimum gap height between the sliding and bearing plates occurs near the middle of the LP side, which was experimentally validated by the witness marks on the bearing plate. In addition, the simulation results suggest that the sliding plate has good stability at high rotational speeds due to the slight variation of the tilting angle of the sliding plate over a cycle.

Nomenclature

Abbreviations

BDC	Bottom dead center
DLC	Diamond-like carbon
DLC + WC	W-doped DLC coating
HP	High-pressure
LP	Low-pressure

Variables

a_p	Acceleration of the piston along its centerline
f_b	Friction coefficient between the piston ball and slipper socket
f_p	Friction coefficient between the piston and cylinder bore
F_a	Reciprocating inertial force of the piston-slipper assembly
F_b	Contact force between the piston ball and slipper socket
F_d	Pressure force from the displacement chamber
F_f	Friction force between the piston and cylinder bore
F_s	Spring force exerted by the spherical cup
$\boldsymbol{F}_c$	Total clamping force
$\boldsymbol{F}_h$	Separating force generated by the fluid film
h	Gap height
h_1, h_2, h_3	Gap heights at three points
h_{max}	Maximum gap height
h_{min}	Minimum gap height
J_p	Piston's moment of inertia about its axis
l	Contact length of the piston within the cylinder bore
l_0	Initial contact length of the first piston
L	Piston length
m	Mass of one piston-slipper assembly
m_p	Piston mass
M_x	Moment component of $\boldsymbol{M}_c$ in the x direction
M_y	Moment component of $\boldsymbol{M}_c$ in the y direction
$\boldsymbol{M}_c$	Moment generated by the total clamping force
$\boldsymbol{M}_h$	Moment generated by the separating force
N_1, N_2	Contact forces between the piston and cylinder bore at two engaging ends
p	Fluid pressure
p_c	Casing pressure of the pump
$p(\varphi_i)$	ith displacement chamber pressure as a function of the angular displacement
r	Radial distance from the coordinate origin
r_b	Piston ball radius
r_p	Piston radius
R	Pitch radius of the kidney-shaped pockets in the sliding plate
R_1	Inner radius of internal sealing land

R_2	Outer radius of internal sealing land
R_3	Inner radius of external sealing land
R_4	Outer radius of external sealing land
R_p	Piston pitch radius
t	Time
v_p	Velocity of the piston along its centerline
V_p	Resultant velocity of the piston relative to the cylinder block
α	Angular span of the kidney-shaped pocket in the sliding plate
β	Swash-plate angle
θ	Angular distance from the y axis
θ_a	Azimuth angle of the minimum or maximum gap height
φ	Angular displacement of the piston from the BDC
μ	Fluid dynamic viscosity
ρ	Fluid density
ω	Rotational speed of the pump
ω_p	Spinning speed of the piston
ω_s	Rotational speed of the sliding plate

Acknowledgements This work was supported by the National Key R&D Program of China (Grant No. 2019YFB2004504), the National Natural Science Foundation of China (Grant No. 52005323), the National Outstanding Youth Science Foundation of China (Grant No. 51922093), the China National Postdoctoral Program for Innovative Talents (Grant No. BX20200210), and the China Postdoctoral Science Foundation (Grant No. 2019M660086). The authors are thankful to research fellow Wunong Hu and senior engineer Yan Zhang, both at AVIC Xi'an Flight Automatic Control Research Institute, for their kind help during tests on the high-speed axial piston pump prototype.

References

1. Ernst M, Vacca A. Hydrostatic vs. hydrodynamic components of fluid pressure in the tribological interfaces of axial piston machines. Tribology International, 2021, 157: 106878
2. Chao Q, Zhang J, Xu B, Huang H, Pan M. A review of high-speed electro-hydrostatic actuator pumps in aerospace applications: challenges and solutions. Journal of Mechanical Design, 2019, 141(5): 050801
3. Guo S, Chen J, Lu Y, Wang Y, Dong H. Hydraulic piston pump in civil aircraft: current status, future directions and critical technologies. Chinese Journal of Aeronautics, 2020, 33(1): 16–30
4. Chao Q, Tao J, Lei J, Wei X, Liu C, Wang Y, Meng L. Fast scaling approach based on cavitation conditions to estimate the speed limitation. Frontiers of Mechanical Engineering, 2021, 16(1): 176–185
5. Hooke C J, Li K Y. The lubrication of slippers in axial piston pumps and motors—the effect of tilting couples. Proceedings of the Institution of Mechanical Engineers. Part C, Journal of Mechanical Engineering Science, 1989, 203(5): 343–350
6. Hashemi S, Kroker A, Bobach L, Bartel D. Multibody dynamics of pivot slipper pad thrust bearing in axial piston machines incorporating thermal elastohydrodynamics and mixed lubrication model. Tribology International, 2016, 96: 57–76
7. Hashemi S, Friedrich H, Bobach L, Bartel D. Validation of a thermal elastohydrodynamic multibody dynamics model of the slipper pad by friction force measurement in the axial piston pump. Tribology International, 2017, 115: 319–337
8. Manring N D, Mehta V S, Nelson B E, Graf K J, Kuehn J L. Scaling the speed limitations for axial-piston swash-plate type hydrostatic machines. Journal of Dynamic Systems, Measurement, and Control, 2014, 136(3): 031004
9. Shi C, Wang S, Wang X, Zhang Y. Variable load failure mechanism for high-speed load sensing electro-hydrostatic actuator pump of aircraft. Chinese Journal of Aeronautics, 2018, 31(5): 949–964
10. Xu B, Zhang J, Yang H. Investigation on structural optimization of anti-overturning slipper of axial piston pump. Science China. Technological Sciences, 2012, 55(11): 3010–3018
11. Jiang J, Wang Z. Optimization and influence of micro-chamfering on oil film lubrication characteristics of slipper/swashplate interface within axial piston pump. Energies, 2021, 14(7): 1961
12. Koç E, Hooke C J. Considerations in the design of partially hydrostatic slipper bearings. Tribology International, 1997, 30(11): 815–823
13. Ma J, Chen J, Li J, Li Q, Ren C. Wear analysis of swash plate/slipper pair of axis piston hydraulic pump. Tribology International, 2015, 90: 467–472
14. Wu H, Zhao L, Ni S, He Y. Study on friction performance and mechanism of slipper pair under different paired materials in high-pressure axial piston pump. Friction, 2020, 8(5): 957–969
15. Rizzo G, Massarotti G P, Bonanno A, Paoluzzi R, Raimondo M, Blosi M, Veronesi F, Caldarelli A, Guarini G. Axial piston pumps slippers with nanocoated surfaces to reduce friction. International Journal of Fluid Power, 2015, 16(1): 1–10
16. Kalin M, Majdič F, Vižintin J, Pezdirnik J, Velkavrh I. Analyses of the long-term performance and tribological behavior of an axial piston pump using diamondlike-carbon-coated piston shoes and biodegradable oil. Journal of Tribology, 2008, 130(1): 011013
17. Schuhler G, Jourani A, Bouvier S, Perrochat J M. Efficacy of coatings and thermochemical treatments to improve wear resistance of axial piston pumps. Tribology International, 2018, 126: 376–385
18. Ye S, Tang H, Ren Y, Xiang J. Study on the load-carrying capacity of surface textured slipper bearing of axial piston pump. Applied Mathematical Modelling, 2020, 77: 554–584
19. Tang H, Ren Y, Kumar A. Optimization tool based on multi-objective adaptive surrogate modeling for surface texture design of slipper bearing in axial piston pump. Alexandria Engineering Journal, 2021, 60(5): 4483–4503
20. Ye S, Zhang J, Xu B, Hou L, Xiang J, Tang H. A theoretical dynamic model to study the vibration response characteristics of an axial piston pump. Mechanical Systems and Signal Processing, 2021, 150: 107237
21. Chao Q, Zhang J, Xu B, Wang Q. Multi-position measurement of oil film thickness within the slipper bearing in axial piston pumps. Measurement, 2018, 122: 66–72
22. Harris R M, Edge K A, Tilley D G. The spin motion of pistons in a swashplate-type axial piston pump. In: Proceedings of the 3rd

Scandinavian International Conference on Fluid Power. Linköping, 1993, 95–111

23. Zhang J, Chao Q, Xu B. Analysis of the cylinder block tilting inertia moment and its effect on the performance of high-speed electro-hydrostatic actuator pumps of aircraft. Chinese Journal of Aeronautics, 2018, 31(1): 169–177
24. Khonsari M M, Booser E R. Applied Tribology: Bearing Design and Lubrication. 2nd ed. Chichester: John Wiley & Sons, 2008, 144–151
25. Xu B, Zhang J, Yang H. Simulation research on distribution method of axial piston pump utilizing pressure equalization mechanism. Proceedings of the Institution of Mechanical Engineers. Part C, Journal of Mechanical Engineering Science, 2013, 227(3): 459–469
26. Xu B, Chao Q, Zhang J, Chen Y. Effects of the dimensional and geometrical errors on the cylinder block tilt of a high-speed EHA pump. Meccanica, 2017, 52(10): 2449–2469
27. Wu W, Xiao B, Hu J, Yuan S, Hu C. Experimental investigation on the air-liquid two-phase flow inside a grooved rotating-disk system: flow pattern maps. Applied Thermal Engineering, 2018, 133: 33–38
28. Ivantysyn R, Weber J. "Transparent pump"—an approach to visualize lifetime limiting factors in axial piston pumps. In: Proceedings of the 9th FPNI PhD Symposium on Fluid Power. Florianópolis: ASME, 2016, V001T01A006
29. Manring N D. Slipper tipping within an axial-piston swash-plate type hydrostatic pump. In: Proceedings of the ASME International Mechanical Engineering Congress and Exposition. Anaheim: ASME, 1998, 169–175
30. Koç E, Hooke C J. Investigation into the effects of orifice size, offset and overclamp ratio on the lubrication of slipper bearings. Tribology International, 1996, 29(4): 299–305
31. Pelosi M, Ivantysynova M. Heat transfer and thermal elastic deformation analysis on the piston/cylinder interface of axial piston machines. Journal of Tribology, 2012, 134(4): 041101
32. Schenk A, Ivantysynova M. A transient thermoelastohydrodynamic lubrication model for the slipper/swashplate in axial piston machines. Journal of Tribology, 2015, 137(3): 031701
33. Li Y, Ji Z, Yang L, Zhang P, Xu B, Zhang J. Thermal-fluid-structure coupling analysis for valve plate friction pair of axial piston pump in electrohydrostatic actuator (EHA) of aircraft. Applied Mathematical Modelling, 2017, 47: 839–858
34. Manring N D, Wray C L, Dong Z. Experimental studies on the performance of slipper bearings within axial-piston pumps. Journal of Tribology, 2004, 126(3): 511–518
35. Chacon R, Ivantysynova M. Advanced virtual prototyping of axial piston machines. In: Proceedings of the 9th FPNI PhD Symposium on Fluid Power. Florianópolis: ASME, 2016, V001T01A036
36. Zhang J, Chao Q, Xu B, Pan M, Wang Q, Chen Y. Novel three-piston pump design for a slipper test rig. Applied Mathematical Modelling, 2017, 52: 65–81